

# The dynamical state of RXCJ1230.7+3439: a multi-substructured merging galaxy cluster

R. Barrena<sup>1,2</sup>, H. Böhringer<sup>3,4</sup>, and G. Chon<sup>4</sup>

<sup>1</sup> Instituto de Astrofísica de Canarias, C/Vía Láctea s/n, E-38205 La Laguna, Tenerife, Spain  
e-mail: rbarrena@iac.es

<sup>2</sup> Universidad de La Laguna, Departamento de Astrofísica, E-38206 La Laguna, Tenerife, Spain

<sup>3</sup> Max-Planck-Institut für extraterrestrische Physik, D-85748 Garching, Germany

<sup>4</sup> Universitäts-Sternwarte München, Fakultät für Physik, Ludwig-Maximilians-Universität München, Scheinerstr. 1, D-81679 München, Germany

Received ; accepted

## ABSTRACT

We analyse the kinematical and dynamical state of the galaxy cluster RXCJ1230.7+3439 (RXCJ1230), at  $z = 0.332$ , using 93 new spectroscopic redshifts of galaxies acquired at the Telescopio Nazionale Galileo and from SDSS DR16 public data. We study the density galaxy distribution retrieved from photometric SDSS multiband data. We find that RXCJ1230 appears as a clearly isolated peak in the redshift space, with a global line-of-sight (LOS) velocity dispersion  $\sigma_v = 1004^{+147}_{-122}$  km s<sup>-1</sup>. Several tests applied to the spatial and velocity distributions reveal that RXCJ1230 is a complex system with the presence of three subclusters, located at the south-west, east and south with respect to the main body of the cluster, containing several bright galaxies (BGs) in their respective cores. Our analyses confirm that the three substructures are in a pre-merger phase, where the main interaction takes place with the south-west subclump, almost in the plane of the sky. We compute a velocity dispersion of  $\sigma_v \sim 1000$  and  $\sigma_v \sim 800$  km s<sup>-1</sup> for the main cluster and the south-west substructure, respectively. The central main body and south-west substructure differ by  $\sim 870$  km s<sup>-1</sup> in the LOS velocity. From these data, we estimate a dynamical mass of  $M_{200} = 9.0 \pm 1.5 \times 10^{14} M_\odot$  and  $4.4 \pm 3.3 \times 10^{14} M_\odot$  for the RXCJ1230 main body and south-west clump, respectively, which reveals that the cluster will suffer a merging characterized by a 2:1 mass ratio impact. We solve a two-body problem for this interaction and find that the most likely solution suggests that the merging axis lies  $\sim 17^\circ$  from the plane of the sky and the subcluster will fully interact in  $\sim 0.3$  Gyr. However, a slight excess in the X-ray temperature observed in the south-west clump confirms a certain degree of interaction already. The comparison between the dynamical masses and those derived from X-ray data reveals a good agreement within errors (differences  $\sim 15\%$ ), which suggests that the innermost regions ( $< r_{500}$ ) of the galaxy clumps are almost in hydrostatical equilibrium. To summarize, RXCJ1230 is a young but also massive cluster in a pre-merging phase accreting other galaxy systems from its environment.

**Key words.** Galaxies: clusters: individual: RXCJ1230.7+3439. X-rays: galaxies: clusters

## 1. Introduction

According to the hierarchical structure formation scenario, Galaxy Clusters (GCs) are the youngest bound systems in our Universe. The cold dark matter model, together with the theory of cosmic inflation predicts the initial conditions for the structure formation (see e.g. [Springel 2005](#)), where clusters form in the deepest potential wells generated by the dark matter (DM) overdensities. GCs contain multiple components. In addition to DM, haloes include baryonic matter in different forms (see e.g. [Allen et al. 2011](#)). Cold and hot gas and non-thermal plasma constitute the intra-cluster medium (ICM), which highly reacts in collision processes, while the galactic component is less affected in mergings events. This multi-component nature allows us to analyse GCs through different wavelengths, given that different physical processes befall in each case. For example, we use X-rays and radio observations to probe the ICM ([Loewenstein 2003](#); [Böhringer & Werner 2010](#); [van Weeren et al. 2019](#)), while visible and infrared data are used to analyse the galactic behaviour (see [Biviano 2000](#), for a review). On the other hand, DM is better studied through weak-lensing techniques ([Umetsu 2020](#)). Therefore, the multi-wavelength observations provide a more complete view about the reality of GCs.

X-ray observations are often used to investigate the dynamical state of GCs. However, optical information is an essential technique to study the dynamics of cluster mergers ([Golovich et al. 2019](#)). The spatial distribution (obtained from photometric observations) and kinematics (retrieved using spectroscopic redshifts) of galaxy members allow us to identify substructures and to analyse possible pre- and post-merging scenarios. Moreover, optical data complement the X-ray information because ICM and galaxies react on different time-scales during a collision ([Roettiger et al. 1997](#)), thus the importance of combining X-ray and optical data. In this context, we analyse in this work the dynamical state of the RXCJ1230.7+3439 (hereafter RXCJ1230) cluster of galaxies using X-ray and optical data.

RXCJ1230 was discovered using X-ray data by [Appenzeller et al. \(1998\)](#) under the designation ATZ98-D219 and by [Böhringer et al. \(2000\)](#) as part of the NORAS survey, with a redshift of  $z = 0.333$ . This cluster has been also detected through its Sunyaev-Zeldovich (SZ) signal in the second Planck cluster catalog ([Planck Col. XXVII 2016](#)). It is also detected in the Northern Sky Cluster Survey ([Gal et al. 2003](#)) and in the Sloan Digital Sky Survey (SDSS) by [Wen et al. \(2009\)](#) and [Hao et al. \(2010\)](#). RXCJ1230 contains a strong X-ray point source in the

North of the cluster, associated with the NVSS 123050+344257 radio galaxy, at the redshift of the cluster.

To date, there is a poor spectroscopic information available in the literature and databases. For instance, only 15 spectroscopic redshifts are reported by SDSS-DR16 within a region of  $15'$  radius with respect to the center of the cluster, insufficient to perform any detailed dynamical study. So, we have recently carried out multiobject spectroscopic observations at the TNG 3.5m telescope obtaining new redshift data for 81 galaxies in the field of RXCJ1230. In addition, we also include photometric information retrieved from SDSS-DR16 and Pan-STARRS1 imaging archives. All these data, together with X-ray information will allow us to investigate the kinematics and dynamics of RXCJ1230, obtaining a satisfactory answer for questions such as, is this a merging cluster?, is it in a pre- or a post- merger phase?, how well X-ray and dynamic mass estimates match?, ... Here, we will clarify the dynamical stage of RXCJ1230.

This paper is organized as follows. We describe the new spectroscopic observations and data samples in Sect. 2. In Sect. 3 we present our results about the selection of galaxy members, velocity and spatial distributions, and substructures. In Sect. 4, we present global properties, dynamical masses of the different structures and a comparison with X-ray properties. In Sect. 5, we analyse the 3D dynamics of the complex and we propose a plausible pre-merging scenario for RXCJ1230. At the end of this paper, in Sect. 6 we summarize our results and expose our conclusions.

In this paper, we have worked assuming a flat cosmology with  $\Omega_m = 0.3$ ,  $\Omega_\Lambda = 0.7$  and  $H_0 = 70 h_{70} \text{ km s}^{-1} \text{ Kpc}^{-1}$ . Under this cosmology, 1 arcmin corresponds to  $287 h_{70}^{-1} \text{ Mpc}$  at the redshift of the cluster.

## 2. Data sample

### 2.1. Optical spectroscopy

We performed multi-object spectroscopic (MOS) observations of RXCJ1230 at the 3.5m TNG telescope in 2020 March, mapping a region of about  $10' \times 10'$  with two MOS masks and including a total of 92 slits. We used the DOLORES spectrograph and the LR-B grism<sup>1</sup>, which offers a wavelength coverage between 370 and 800 nm with a spectral resolution of  $2.75 \text{ \AA}$  per pixel. The total integration time was 3600 s per mask, divided in two exposures of 1800 s each. The combination of these two acquisitions allowed us to correct the spectra from cosmic rays.

The spectra were extracted using standard IRAF<sup>2</sup> packages. The radial velocity computation was performed using the cross-correlation technique developed by Tonry & Davis (1979) and implemented as the task RVSAO.XCSAO in IRAF environment. This procedure correlates the features detected in the observed spectra (mainly Ca H and K doublet,  $H_\delta$ , G band, MgI, in absorption and the most relevant emission lines such as OII, OIII doublet,  $H_\alpha$ ,  $H_\beta$  and  $H_\delta$ ) with that present in the templates spectra. We used five different reference spectra of the Kennicutt Spectrophotometric Atlas of Galaxies (Kennicutt 1992), for 5 different morphologies (Elliptical, Sa, Sb, Sc and Irr types). So, this procedure yields radial velocity estimates and the corresponding errors due to the correlation technique applied. After rejecting the spectra with lower signal-to-noise ratio (SNR), we

obtained 81 spectroscopic redshifts. In addition, we also consider 12 redshifts retrieved from the SDSS DR16 spectroscopic database present in the region sampled by the two masks field of view around RXCJ1230.

A detailed comparison between redshifts derived from multiple measures of the same target (obtained from two different estimation in the two masks, or even between SDSS redshift and our estimate), we see that the nominal velocity errors provided by the cross-correlation technique are too small. Therefore, in order to convert this error into a realistic value, considering systematic errors, we need to multiply them by a factor of 2 (see e.g. Boschin et al. 2013).

Our spectroscopic catalogue includes a total of 93 galaxy redshifts in a region of  $9' \times 10'$  arcmin (see Fig. 1, left panel). The MOS mask design was initially planned to cover more efficiently the densest galaxy regions. So, the majority of the spectroscopic redshifts follows an elongated region in the NE-SW direction. Our full redshift sample presents a median SNR and  $cz$  error of 8 and  $82 \text{ km s}^{-1}$ , respectively. We detect 12 star forming galaxies, characterized by the presence of the [OII] emission line.

### 2.2. Optical photometry

We complement our redshift sample with photometric information retrieved from SDSS DR16 database. We consider  $dered\ r'$  and  $i'$  magnitudes<sup>3</sup>. Galaxy counts in this region reveals the photometric SDSS sample is  $\sim 90\%$  complete for galaxies down to magnitude  $r' = 21.5$ , which is in agreement with the mean SDSS DR12 depth estimations<sup>4</sup>.

Pan-STARRS1 data archive<sup>5</sup> was only used in order to retrieve RGB images and overplot density contours and galaxies with spectroscopic redshifts (see Fig. 1).

Comparing the spectroscopic and photometric samples in the area covered by MOS masks, we find that the completeness of the spectroscopic sample is  $\sim 55\%$  for galaxies down to magnitude  $r' = 21$ . However, we are able to obtain redshifts even for galaxies with  $r' > 21.5$ .

Table 1 lists the full spectroscopic sample considered in this work (see also Fig. 1). Col. 1 lists an ID number (cluster members are indicated), Cols. 2 and 3 reports the equatorial coordinates of galaxies in J2000 system, Col. 4 the heliocentric radial velocity ( $v = cz$ ) with errors ( $\Delta v$ ), and Cols 5 and 6, the complementary photometric information ( $r'$  and  $i'$   $dered$  magnitudes) retrieved from SDSS DR16. The last column includes some comments regarding particular features of some galaxies.

### 2.3. Complementary X-ray data

The XMM-Newton observations (ID 0841900101) and their data analysis, which complete our multiwavelength study, are described in detail in Böhringer et al. (2022). Here, we only use X-ray data for a qualitative and morphological analysis. We use the 0.5 to 2.0 keV band, which provides the highest signal to noise above the background. In the present work we perform two minor modifications to the raw X-ray image. First, we remove the point sources and emission from NVSS 123050+344257 radio galaxy (ID 78) by masking them with circular apertures of 10-20 pixels radius; Second, we smooth the original image using a Gaussian filter with a FWHM=12 arcsec. After this process, we

<sup>1</sup> See <http://www.tng.iac.es/instruments/lrs>

<sup>2</sup> IRAF (<http://iraf.noao.edu/>) is distributed by the National Optical Astronomy Observatories, which are operated by the Association of Universities for Research in Astronomy, Inc., under cooperative agreement with the National Science Foundation.

<sup>3</sup>  $dered$  magnitudes are the extinction-corrected values following Schlegel et al. (1998) reddening maps.

<sup>4</sup> see [https://www.sdss.org/dr12/imaging/other\\_info/](https://www.sdss.org/dr12/imaging/other_info/)

<sup>5</sup> see <https://ps1images.stsci.edu/cgi-bin/ps1cutouts>

**Table 1.** Velocity catalogue of 93 galaxies measured spectroscopically in the RXJ1230 field.

ID	R.A. & Dec. (J2000) R.A.=12:mm:ss.ss Dec.=+34:mm:ss.ss		$v \pm \Delta v$ (km s <sup>-1</sup> )	$r'$	$i'$	Notes
1*	30:17.02	34:22.3	98389 ± 102	19.69	19.25	
2	30:19.11	40:59.0	90506 ± 77	19.78	19.22	
3*	30:22.18	36:37.2	99651 ± 62	18.86	18.22	
4*	30:22.86	36:44.4	100135 ± 79	20.66	20.14	
5*	30:23.72	39:40.5	97351 ± 94	19.21	18.77	ELG
6	30:23.17	40:41.3	118366 ± 76	19.55	19.12	ELG
7*	30:24.45	40:01.7	97405 ± 82	20.63	20.07	
8	30:25.53	40:28.5	90865 ± 85	19.04	18.43	ELG
9*	30:26.53	36:01.1	100299 ± 68	20.39	19.89	
10*	30:26.00	37:23.0	100012 ± 103	21.04	20.47	
11*	30:27.68	40:49.8	98300 ± 100	20.75	20.33	
12*	30:27.16	37:30.3	98085 ± 31	20.22	19.68	
13*	30:28.11	34:51.2	98441 ± 142	20.57	20.16	
14*	30:28.03	35:42.0	99284 ± 78	21.07	20.75	
15*	30:28.63	37:35.5	99494 ± 60	19.73	19.16	
16*	30:28.61	37:41.4	100177 ± 85	19.53	18.97	
17*	30:28.36	37:52.8	97806 ± 98	20.80	20.37	
18*	30:28.78	40:12.7	98013 ± 76	20.46	19.87	
19	30:28.96	41:20.4	118244 ± 55	20.15	19.52	ELG
20*	30:29.28	38:01.3	98445 ± 70	20.46	19.83	
21*	30:29.54	38:06.9	97959 ± 16	18.07	17.50	BG-W (2)
22*	30:30.55	38:01.4	98007 ± 18	17.90	17.33	BG-W (1)
23	30:31.78	41:28.7	90405 ± 145	20.24	19.61	
24*	30:32.80	38:11.5	98538 ± 92	20.59	20.10	
25*	30:33.48	38:19.5	100904 ± 116	19.95	19.51	
26*	30:33.73	38:32.7	98418 ± 54	19.53	19.03	
27*	30:35.37	38:27.4	98488 ± 86	20.60	20.17	
28	30:36.83	38:41.1	139900 ± 100	21.98	21.71	ELG
29*	30:37.75	36:16.5	101460 ± 85	19.92	19.37	
30*	30:38.15	34:58.3	99530 ± 100	20.70	20.21	
31*	30:38.52	35:48.8	100702 ± 118	20.72	20.14	
32*	30:38.80	39:55.4	102345 ± 100	19.86	19.20	
33*	30:38.19	36:18.8	98484 ± 34	20.67	20.09	
34*	30:38.21	38:06.3	100291 ± 25	19.92	19.38	
35	30:39.41	34:36.2	86666 ± 111	21.04	20.55	
36*	30:39.73	39:22.6	99681 ± 51	20.28	19.68	
37	30:39.18	35:55.6	156900 ± 100	21.89	21.63	ELG
38*	30:39.97	39:32.3	101073 ± 115	19.72	19.14	
39*	30:40.75	35:29.6	99991 ± 93	20.25	19.63	
40*	30:41.59	34:12.3	98373 ± 81	19.33	18.94	
41*	30:41.64	39:51.4	99151 ± 67	20.61	20.13	
42	30:41.18	41:48.5	112903 ± 63	20.32	20.12	ELG
43*	30:42.20	41:40.3	101134 ± 182	19.91	19.33	
44*	30:42.48	36:13.5	98196 ± 89	20.39	19.85	
45	30:42.48	36:30.5	157618 ± 100	20.92	20.19	ELG
46*	30:42.57	37:31.2	99913 ± 157	20.53	20.01	
47*	30:42.12	38:01.7	99099 ± 61	20.21	19.67	
48*	30:42.47	40:24.3	100238 ± 98	19.70	19.22	
49	30:43.81	35:12.0	103864 ± 68	18.19	17.72	
50*	30:43.73	36:27.2	100334 ± 105	20.35	19.76	
51*	30:43.56	36:06.1	100379 ± 107	20.55	20.12	
52*	30:43.93	39:21.2	100007 ± 35	20.47	19.94	
53*	30:44.95	38:46.7	99914 ± 107	20.58	20.07	
54	30:44.83	37:50.8	112918 ± 101	20.07	19.80	ELG
55*	30:44.47	39:38.7	100638 ± 87	19.49	18.87	
56*	30:44.82	40:58.1	99794 ± 62	20.17	19.52	
57*	30:45.65	40:18.0	99754 ± 88	20.80	20.28	
58*	30:45.57	35:41.8	102128 ± 68	20.45	19.90	
59*	30:45.92	38:19.0	100622 ± 70	19.60	19.06	
60*	30:45.78	39:26.3	100064 ± 28	18.49	17.89	BCG
61*	30:47.98	36:56.7	99109 ± 78	18.69	18.10	BG-S
62*	30:47.93	37:03.7	96570 ± 100	20.80	20.74	ELG
63*	30:47.78	43:26.5	100517 ± 86	19.54	18.98	
64*	30:48.41	37:11.3	99457 ± 77	20.32	19.75	
65*	30:48.35	36:48.7	99042 ± 108	21.82	21.26	
66*	30:48.52	36:58.9	99102 ± 145	21.27	20.93	
67*	30:48.83	37:07.7	99103 ± 55	20.68	20.17	
68*	30:48.50	38:11.8	99959 ± 83	19.55	19.06	
69*	30:48.41	38:47.2	102209 ± 60	21.19	20.52	
70*	30:48.66	39:08.4	99497 ± 63	21.17	20.57	
71*	30:48.60	42:27.7	99761 ± 63	19.60	19.08	

**Table 1.** Continued.

ID	R.A. & Dec. (J2000) R.A.=12:mm:ss.ss Dec.=+34:mm:ss.ss		$v \pm \Delta v$ (km s <sup>-1</sup> )	$r'$	$i'$	Notes
72	30:48.06	42:37.2	63400 ± 100	18.78	18.44	
73*	30:49.14	37:17.7	98558 ± 88	20.36	19.98	
74*	30:49.72	40:33.5	99387 ± 52	19.72	19.07	
75*	30:49.81	42:10.1	101085 ± 77	21.03	20.39	
76*	30:49.43	41:25.4	99249 ± 37	20.57	20.03	
77*	30:50.36	42:01.2	101520 ± 100	20.58	20.11	
78*	30:50.67	42:53.5	100907 ± 98	18.51	17.93	NVSS RG
79	30:51.83	36:20.4	90272 ± 145	21.20	20.68	
80*	30:51.66	38:59.0	101592 ± 49	19.63	18.94	ELG
81*	30:51.07	40:48.1	100908 ± 71	20.73	20.18	
82*	30:51.03	38:27.4	96834 ± 39	20.35	19.83	
83*	30:52.32	43:18.4	100868 ± 97	20.12	19.64	
84*	30:53.33	41:54.3	102042 ± 90	19.23	18.81	ELG
85*	30:54.56	37:42.9	101422 ± 92	20.90	20.52	
86	30:54.99	41:23.5	40650 ± 100	21.49	21.04	
87*	30:55.30	41:31.8	99746 ± 48	18.68	18.10	
88	30:56.48	41:46.3	92621 ± 165	20.46	19.77	
89*	30:57.96	39:23.5	101676 ± 54	18.56	17.92	
90*	30:59.34	39:13.9	100226 ± 19	19.51	18.92	
91*	31:01.05	38:09.1	97834 ± 17	18.54	17.93	
92*	31:03.70	39:08.1	99064 ± 20	18.64	18.05	
93*	31:04.67	40:08.7	99113 ± 45	18.13	17.54	BG-E

Note: asterisk in column 1 (ID) indicates the galaxies selected as cluster members.

obtain the X-ray surface brightness maps plotted as contours in the right panel of Fig. 1, overlaid to an optical colour composite image from the PanSTARSS survey (similarly as shown in Fig. 2 by Böhringer et al. 2022).

Analysis of the X-ray spectra in the different substructures of the cluster yields an intracluster plasma temperature of  $4.7 \pm 0.4$  keV for the central main component,  $4.4 \pm 0.6$  keV for the south-western subcluster and  $3.3^{+0.7}_{-0.6}$  keV for the eastern structure (Böhringer et al. 2022). They also find that the temperature profile for the main component is not very steep with a polytropic index between isothermal and 1.2 and all components have no cool cores. From the temperature and the shape of the intracluster gas distribution Böhringer et al. (2022) obtained a hydrostatic mass estimate of the cluster components. They combined this result with mass estimates based on scaling relations of cluster mass with X-ray temperature, with X-ray luminosity, with total gas mass and with  $Y_X$  (the product of temperature and gas mass) to arrive at a consistent picture for the mass estimation. See Sect. 4.1 for a summary of X-ray mass and a comparison with the dynamical one.

### 3. Analysis and results

#### 3.1. Member selection and global properties

To select cluster members out of the 93 galaxies in our spectroscopic sample, we follow a method based on the galaxy position in the 2D projected phase space ( $r$ ,  $cz$ ), where  $r$  is the projected distance from the cluster center, and  $cz$  is the galaxy line-of-sight velocity (see Fig. 3, top panel).

To minimize the presence of interlopers, we apply a  $2.7\sigma_v$  clipping in the  $cz$  coordinate, taking into account the radial profile of the expected velocity dispersion (Mamon et al. 2010). Therefore, we apply an iterative method which, in a first step, we find the mean significant peak in the velocity distribution ( $v_0 = < cz_0 >$ ) and estimate first velocity dispersion ( $\sigma_0 = \sigma_{v,0}$ ) using the *rms* estimator. Considering these two values, in a second step,



we select cluster members as galaxies with  $v < v_0 \pm 2.7\sigma_0$ . In the final step, we refine the estimation of the mean  $cz$  of the cluster and re-evaluate the velocity dispersion  $\sigma_v$  of the cluster. This simple three-step procedure yields stable and converging values of  $\bar{v}$  and  $\sigma_v$  in a fourth and subsequent steps. Fig. 2 shows the redshift distribution of the galaxies listed in Tab. 1.

In this way, we select 77 galaxy members with a  $\bar{v} = 99658 \pm 161 \text{ km s}^{-1}$  ( $z = 0.3324$ ) with an  $rms$  of  $969 \pm 130 \text{ km s}^{-1}$  (errors at 95% c.l.) in the cluster rest frame. In order to verify these values, we also apply the bi-weight scale estimator (Beers et al. 1990) considering the 77 redshifts. So, we find a  $\sigma_v = 1004^{+147}_{-122} \text{ km s}^{-1}$ . Thus, both  $rms$  and bi-weight estimators produce results in perfect agreement within errors. However, in order to check how robust this estimate is, we study the variation of  $\sigma_v$  with the distance to the center of the cluster, which is taken to be the brightest cluster galaxy (BCG<sup>6</sup>) position. Fig. 3, bottom panel, shows that the integral  $\sigma_v$  profile is flat beyond 0.7 Mpc, suggesting that the estimation of the  $\sigma_v$  is robust for the whole cluster. In the following analyses we use the bi-weight estimator given its robustness in cases where the statistics clearly departs from the Gaussian distribution. In addition to the 77 members, we detect 6 galaxies in the foreground and 10 in the background of RXCJ1230.

Another remarkable effect that we find is a clear dependence of the mean velocity with the clustercentric distance (see Fig. 3, middle panel). We notice that the inner and central region shows higher mean velocity, while regions surrounding the main body exhibit velocities up to  $500 \text{ km s}^{-1}$  lower.

The BCG of RXCJ1230 (the ID 60) presents a velocity of  $100064 \pm 28 \text{ km s}^{-1}$ , which is about  $310 \text{ km s}^{-1}$  higher respect to the mean velocity of the cluster. In addition to the BCG, with magnitude  $r' = 18.49$ , we also detect two galaxies even brighter (IDs 22 and 21, with  $r' = 17.90$  and  $18.07$ ) located at the south-west. Besides these bright galaxies (BGs), we also identify two galaxies more, very bright and showing BCG features. One of them is located to the south (the ID 61, with  $r' = 18.69$ ), and another to the east (the ID 93, with  $r' = 18.13$ ). As Fig. 1 shows, the BCG and all BGs are very close to the X-ray peaks as recovered from XMM-Newton data. The BCG is coincident with the main (and central) body of the cluster, while the BG-W(1) and BG-W(2) are very close to the south-west X-ray peak. In a similar way, the BG-S is almost coincident with a small elongation of the X-ray surface brightness toward the south, and the BG-E is placed in the maximum of a weak X-ray emission located to the east of the cluster. As we discuss in following sections, each one of these BGs is linked to a corresponding substructure, configuring a complex multi-substructure cluster.

Additionally, to this set of BGs, we detect 12 galaxies showing [OII] emission lines, but only 4 of these galaxies are cluster members. The SNR and the spectral resolution of our data allow us to detect [OII] lines with equivalent width  $> 8 \text{ \AA}$ . These emission line galaxies (ELGs; star-forming galaxies) are the IDs 5, 62, 80 and 84, and show [OII] equivalent width of 15, 95, 12

and  $18 \text{ \AA}$ , respectively. The ELG members represent the 5.2% of the cluster members in our sample. This fraction indicates that the star-forming processes have been quenched in RXCJ1230, which is in agreement with a presence of high galaxy density environments with ICM showing high  $T_X$  (Laganá et al. 2008).

### 3.2. Velocity field

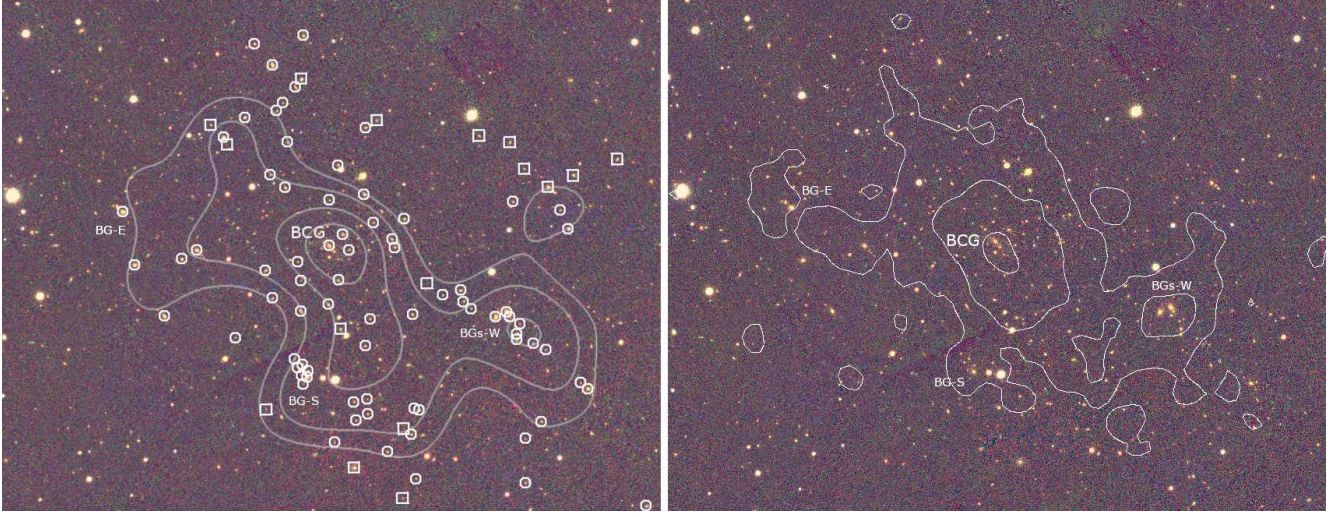
Deviations from Gaussianity in the radial velocity distributions are clear indicators that clusters present substructures (see e.g. Ribeiro et al. 2011). In order to check whether the velocity distribution of RXCJ1230 follows a Gaussian shape, we use two profile estimators, the skewness and kurtosis indexes. Positive skewness indicates the distribution is skewed to the right, with a longer tail to the right of the distribution maximum, while negative skewness indicates that the distribution is shifted and tailed to the left. On the other hand, positive values of the kurtosis indicate distributions presenting thinner tails (leptokurtic) than the normal distribution, while negative values indicate distributions with fatter tails (platykurtic). In our case, we obtain  $-0.038$  and  $-0.532$  for the skewness and kurtosis, respectively. These values suggest that the velocity distribution follows a slightly flatter shape than a normal one, and it is quite symmetric. This implies that probably most of the substructures are placed close to the plane of the sky and no significant velocity deviations are expected in the radial component (along the line of sight).

### 3.3. 2D galaxy distribution

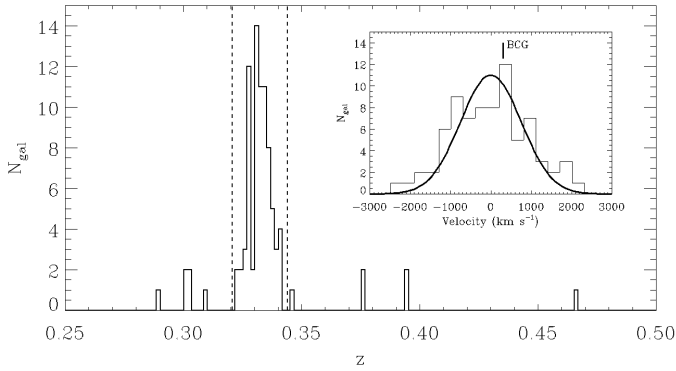
Given that our spectroscopic sample suffers from magnitude incompleteness and does not map the whole cluster field, we also adopt the photometric SDSS DR16 catalogues. Using the  $r'$  and  $i'$  SDSS DR16 photometry in a region of  $12.4' \times 9.6'$ , we construct the  $(r' - i' \text{ vs } r')$  colour magnitude relation (CMD; see Fig. 4) and select likely members from there. First, we fit a red sequence (RS) to the spectroscopically confirmed members by fixing the slope to  $-0.028$  following prescription detailed in Barrena et al. (2012). So, we obtain  $r' - i' = -0.028 \times r' + 1.118 (\pm 0.05)$ . Then, in order to select both likely early-type members (placed in the RS) and galaxy members residing in the green valley and blue-cloud (below the RS) in the CMD of the cluster (Eales et al. 2018), we select the locus defined by the  $RS \pm 3 \times rms$  as upper limit and  $-0.1615 \times r' + 3.37$  as lower limit in  $r' - i'$ , respectively. In addition, we select galaxies down to  $r' = 22.2$ . This locus in the CMD selects 618 likely galaxy members as complete as possible (dashed lines in Fig. 4) in the region considered.

Fig. 1, left panel, shows the contour levels of the isodensity galaxy distribution of likely member. This map has been obtained by evaluating the cumulative contribution of 618 Gaussian profiles (with  $\sigma = 1 \text{ arcsec}$  width) centred on each individual members in a grid of  $245 \times 200$  points. From this study we can assess that the cluster presents a central high density clump (the main body) and the BCG (ID 60) coincident with the highest density peak. A secondary and very dense clump is toward the south-west and two very BGs (IDs 22 and 21) are positioned very close to its corresponding peak. The isodensity contours show a clear elongation from the main body of the cluster to the south. This concentration of galaxies shapes a third small substructure toward the south also containing a BG (ID 61). And finally, a fourth galaxy clump, not so clear in the isodensity contours but also containing a BG (ID 93) is located eastward. Thus, we detect three galaxy clumps (toward the south-west, south and east, respectively, and following the order of a decreasing

<sup>6</sup> Note that the BCG is not strictly the brightest galaxy of this complex cluster. The BCG is the brightest galaxy in the main body and more massive clump of galaxies, and lies very close to the X-ray peak emission and the maximum of galaxy isodensity distribution (see Fig. 1). There are other four galaxy members even brighter than the BCG in RXCJ1230 (see Tab. 1 and Figs. 1 and 4), lying in the surrounding subclusters. These four bright galaxies are labeled as BGs in order to differentiate them from the actual BCG. Probably, these four galaxies can also be considered as BCGs of their respective subclusters, but we label them as BGs to keep the notation more clear and a less confusing reading.



**Fig. 1.** *Left panel:* RGB colour composite image obtained by combining  $g'$ -,  $r'$ - and  $i'$ -band images of  $13' \times 10'$  field of view from Pan-Starrs1 public archive. Circles and squares correspond to galaxy members and non-members, respectively, obtained from our spectroscopic observations and SDSS-DR16 spectroscopic database. Superimposed, we also show the contour levels of isodensity galaxy distribution of likely members (see Sect. 3.3). *Right panel:* The same RGB image but overplotting the contour levels of the XMM-Newton image corresponding to the observation ID 0841900101. The X-ray contours have been obtained after smoothing the original image using a Gaussian filter with  $\sigma = 6$  arcsec. Point sources and emission from NVSS 123050+344257 radio galaxy (ID 78) have been removed masking them with circular apertures of 10-20 pixels radius. In both panels, the BCG and bright galaxies (BGs) are also marked. North is up and East is left.



**Fig. 2.** Galaxy redshift distribution. Dashed vertical lines delimit the redshift range including 77 galaxy members assigned to RXCJ1230 according to  $2.7\sigma_v$  clipping. Superimposed, the velocity distribution, in the cluster rest frame, of the 77 cluster members selected. Black curve represents the reconstruction of the velocity distribution as a Gaussian profile, considering the  $\sigma_v$  computed using the biweight estimator and assuming all the galaxies belonging to a single system. The velocity corresponding to the BCG is also marked.

density) surrounding a very dense main cluster. Tab. 2 lists the precise positions and global properties for these four significant galaxy clumps.

We remark that the external regions of RXCJ1230 are particularly rich of substructures. The substructure configuration reported here using optical data, characterized by a central main body with three substructures around it completely agrees with that observed and reported by Böhringer et al. (2022) using X-ray data retrieved by XMM-Newton. As Fig. 1 shows, the galaxy density contours (left panel) and X-ray surface brightness profile (right panel) are almost coincident and follow the same shape.

### 3.4. Spatial-velocity correlations

One of the most useful tools to test the existence of substructures is the study of possible spatial-velocity correlations. In this work, we use different techniques to analyse the structure of RXCJ1230 combining positions and velocities of galaxy members.

The presence of internal structures clearly influences the cluster velocity field. So, in a first step, in order to investigate the RXCJ1230 complex, we divide galaxies in two samples. We search for possible bimodality through the presence of gaps in the velocity distribution, which could cause drops in the galaxy counts for some particular bins of the velocity histogram (see as an example Fig. 4 in Barrena et al. (2007) for a clear bimodal configuration of Abell 773). In our case, the most important drop is that detected around  $-500 \text{ km s}^{-1}$  (see Fig. 2, inner panel). Considering this drop of galaxy counts around  $-500 \text{ km s}^{-1}$  as a possible frontier between two separate galaxy subsamples, we study the spatial distribution of galaxies with  $v < -500 \text{ km s}^{-1}$  and  $v \geq -500 \text{ km s}^{-1}$ , respectively. We detect no differences between these two galaxy subsets and both populations are homogeneously distributed in space, which suggests that this drop in the velocity histogram is not representative of individual galaxy clumps.

As a second approach, similarly as we proceeded previously, we divide galaxy velocity sample in two sets. One subset containing low velocities with  $v < \bar{v}$ , and a second subset with high velocities ( $v > \bar{v}$ ). In other words, the low and high velocity subsamples correspond to galaxies with negative and positive velocities respect to the mean one in the cluster velocity rest frame (see inner panel of Fig. 2). We check the difference between the two distributions of galaxy positions. Fig. 5 shows that low and high velocity galaxies are segregated, as we advance in Sect. 3.1. While high velocity galaxies (red contours) shape the main body of the system, the low velocity galaxies (blue contours) are placed in the three surrounding substructures. This fact can also be noticed in Fig. 3 (middle panel), where  $\langle v \rangle$  takes values



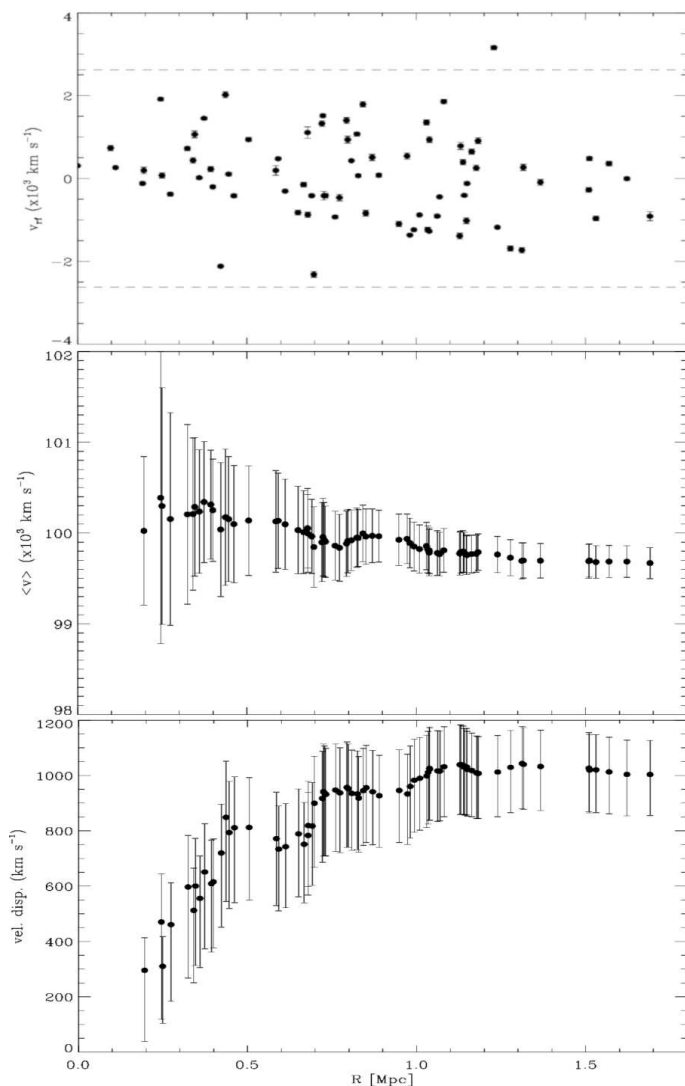


**Fig. 3.** Top panel: rest frame velocity versus projected distance to the cluster centre for the 77 galaxy members selected. The cluster centre is assumed to be the position of the BCG. Middle and bottom panels: Integral profiles and LOS velocity dispersion, respectively. These values are computed by considering all galaxies within that radius. The first value computed is estimated from the first five galaxies closest to the centre. The error bars are at the 68% c.l.

about  $100200 \text{ km s}^{-1}$  for distances  $\sim 0.3 - 0.4 \text{ Mpc}$  and  $99700 \text{ km s}^{-1}$  at  $> 1.2 \text{ Mpc}$ .

We carry out a second test for checking this spatial-velocity segregation. We combine galaxy velocities and positions by computing the  $\delta$ -statistics using the Dressler & Schectman (DS) test (Dressler & Schectman 1988), which looks for groups of galaxies showing deviations from the local velocity mean, or with velocity dispersion that differs from the global one. If one assumes a random distribution of velocities, one would expect such deviations to be proportional to the number of galaxy members,  $\Delta \sim N$ , for clusters without substructure or clusters with substructures with similar velocity dispersion and relative movement in the line of sight with respect their main bodies. On the other hand, one would expect  $\Delta > N$  for clusters with substructures showing relative movements in the line of sight well differentiated from the main body, and/or even subclusters with lower velocity dispersion respect the main cluster. We find a cumulative deviation of  $\Delta = 65$  (at the 95% c.l., as estimated

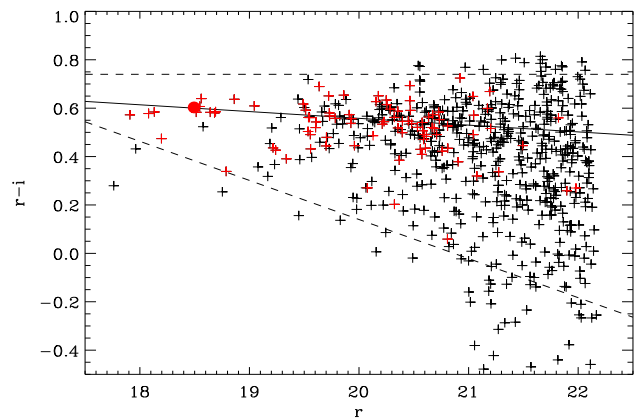


**Fig. 4.** Colour magnitude diagram ( $r' - i', r'$ ) of galaxies in a region of  $12.4' \times 9.6'$ . Red symbols correspond to galaxy members confirmed spectroscopically (red dot corresponds to the BCG of the cluster). Solid line represents the red sequence defined as the densest locus in this diagram, which follows the linear fit  $r' - i' = -0.028 * r' + 1.118$ . Dashed lines delimit the region which enclose the RS and the blue cloud in this diagram. Galaxies included in this region are considered likely members, which are used to obtain the isodensity galaxy distribution shown in Fig. 1.

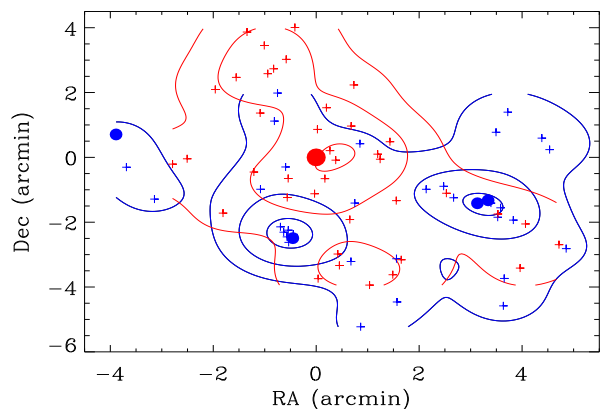


**Fig. 5.** Isodensity contours of spectroscopically confirmed galaxy members. Blue contours corresponds to the 2D distribution of galaxies with negative velocity with respect to the mean one in the cluster rest frame (see Fig. 2, inner panel). Similarly, red contours show isodensity levels for galaxies with positive velocity respect the mean cluster velocity. This plot is centred on the BCG, marked with a red big dot. Blue dots correspond to BGs belonging to the corresponding clumps. Red and blue contours are plotted at the same density level.

by computing 1000 Monte Carlo simulations), which is a value comparable to the number of members (77). This suggests that RXCJ1230 presents all its substructures moving with no significant deviations in the line of sight component respect the main cluster body in agreement with our finding in section 3.2. In addition, the  $\Delta$  value shows that no group has been detected with velocity dispersion very different from that of the whole cluster. However, the cumulative  $\Delta$  is unable to provide information on the presence of possible individual galaxy clumps. This issue is explored in the following using the individual  $\delta$  associated to each galaxy position and also obtained through the DS test.

Fig. 6 illustrates the  $\delta$ -statistics combined with the spatial distribution of the 77 cluster members. Around each point a

square is plotted with side proportional to  $\exp(\delta_i)$ . So, the larger square, the larger is the deviation ( $\delta$ ) of the local mean velocity from the global mean. Red squares correspond to galaxies with  $\delta_i < \bar{\delta}_i$  (where  $\bar{\delta}_i$  is the mean  $\delta_i$  deviation of the 77 cluster members), while blue represents members with deviations  $\delta_i > \bar{\delta}_i$ . This plot shows that the most important substructures is mainly located toward the east and south-west from the main body of the cluster. The galaxies of these groups present higher deviations than galaxies in the main body (center). The main advantage of this method is that no *a priori* selections or assumptions about the positions of subclumps have to be imposed. Therefore, this finding is more parameter independent and so more robust.

To summarize, the study of the individual  $\delta$  of the DS test provides us with a valuable proof of the presence of substructures in the periphery of the cluster supported by high deviations from the mean velocity of the cluster in the external zones. This finding is in agreement with what we find in the 2D spatial distribution (see Sect. 3.3). In addition, the cumulative  $\Delta$  is comparable to the number of cluster members, which suggests that no large relative movement of these substructures are expected in the radial component. Therefore, in agreement with what we find in Sect. 3.2, relative movements of subclusters respect the main body should be (nearly) contained in the plane of the sky.

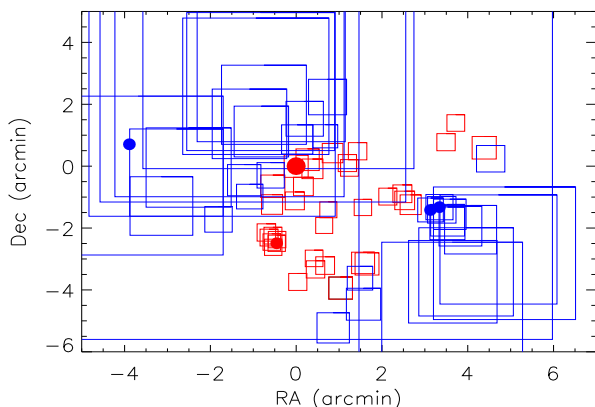


**Fig. 6.** Spatial distribution of the 77 cluster members, each marked by a square. The size of squares is proportional to  $\exp(\delta_i)$  computed using the  $\delta_i$  deviations obtained in the DS test. Red and blue squares separate populations showing deviations lower and higher than  $\bar{\delta}_i$ , respectively. BGC and BG positions are marked with dots.

With the aim of identifying individual galaxies belonging to each substructure, we use a new 3D diagnostic test. We apply a 3D version of the Key's Mixture Model algorithm (KMM; Ashman et al. 1994) in order to separate different components in velocity space. The KMM algorithm estimates the probability that a given galaxy belongs to a given component in an iterative procedure. At the end, the algorithm produces a list of galaxies associated with the cluster main body and with each additional substructure. However, it needs to start from an initial input configuration. In order to minimize the dependence of the final results of probabilities on the initial guess input, we run KMM with several (more than ten) initial randomly allocations to a three galaxy populations, equally composed by 25, 25 and 24 galaxies (the three easternmost galaxies have been excluded from this test given the redshift undersampling in this region<sup>7</sup>). The final result was always the same, converging into a very stable solution. The output

<sup>7</sup> Including a fourth galaxy clump with the three easternmost galaxies does not produce a reliable KMM test result.

set of probabilities fits always a three-group partition, assigning 9 and 7 galaxies to the south-west and south substructures, respectively, with  $>95\%$  probabilities, according to the likelihood ratios obtained from KMM test. The rest of the galaxies are assigned to the main cluster body. This galaxy allocation, for the main body and the two substructures (south-west and south), is shown in Fig. 7. On the other hand, the analysis of the  $p$ -value probability to obtain this KMM result by chance is lower than 0.001 ( $< 0.1\%$  probability). The substructure to the east was not identified through this technique mainly due to the lack of redshift information in this zone. However, the DS test shows high  $\delta_i$  deviations in the surroundings of this region, around  $(-3', 1')$  position in Fig. 6.

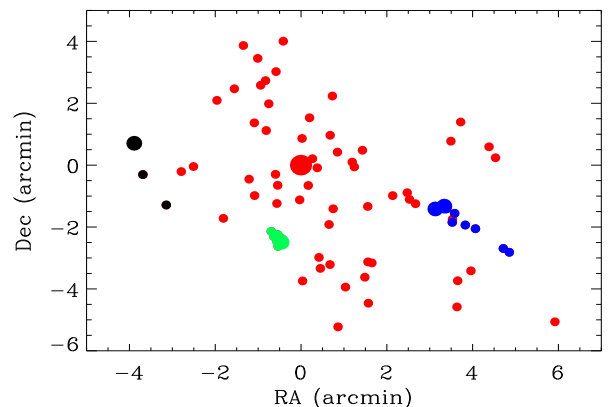


**Fig. 7.** Spatial distribution on the sky of the 77 cluster members. The 9 blue and 7 green dots correspond to the galaxies belonging to the south-west and south substructures identified with  $> 95\%$  probability using the KMM procedure. Red dots correspond to galaxy members being part of the cluster main body with different probabilities following the same algorithm. Black dots correspond to galaxies selected manually as part of the eastern clump according to their space-velocity segregation (see Fig. 5). Big dots mark the BCG and BG.

#### 4. Dynamical mass of RXCJ1230

On the basis of the previous section, we can conclude that RXCJ1230 is formed by three substructures, spatially well separated in the sky. The main substructure is placed to the south-west with respect to the main body of the cluster, and contains two very bright galaxies, the BGs-W (1 and 2). A second substructure is located toward the south, which resembles a very compact group of galaxies dominated by a very bright galaxy, the BG-S. In addition, the spatial distribution of galaxies and the X-ray surface brightness map suggest also the presence of a third clump located to the east and containing a BG.

Although RXCJ1230 is in a phase of interaction, the main system and the three surrounding substructures are still well separated and the 2D galaxy density distribution and BGs well match with their correspondings X-ray peaks. Thus, we can assume that RXCJ1230 is in a pre-merging phase. Moreover, no shock fronts are detected in the X-ray surface brightness map, which are very commonly formed after collisions. So, it is reasonable to assume that each substructure has not yet collided and is roughly in dynamical equilibrium, which allows us to compute virial quantities and estimate the mass of the whole cluster as the sum of the individual subclump masses.

**Table 2.** Positions and global properties for the whole cluster and the four galaxy clumps detected in RXCJ1230.

Structure	R.A. & Dec. (J2000) R.A.=12:mm:ss.ss Dec.=+34:':"	$N_{gal}$	$\bar{v}$ (km s <sup>-1</sup> )	$\sigma_v$ (km s <sup>-1</sup> )	$r_{200}$ ( $h_{70}^{-1}$ Mpc)	$M_{200}$ ( $\times 10^{14} M_{\odot}$ )	$M_{500}$ ( $\times 10^{14} M_{\odot}$ )
Global	30:45.78 39:26.3	77	99658 $\pm$ 161	1004 $^{+147}_{-122}$	–	14.1 $\pm$ 3.8	9.0 $\pm$ 2.3
Centre	30:45.78 39:26.3	58	99967 $\pm$ 161	999 $\pm$ 160	$\sim$ 1.8	9.0 $\pm$ 1.5	5.6 $\pm$ 1.0
South-West	30:30.55 38:01.4	9	98810 $\pm$ 126	792 $\pm$ 230	$\sim$ 1.5	4.4 $\pm$ 3.3	2.7 $\pm$ 2.0
East	31:04.67 40:08.7	3	$\sim$ 99468	$\sim$ 500	$\sim$ 0.8	$\sim$ 1	$\sim$ 0.7
South	30:47.98 36:56.7	7	99090 $\pm$ 192	< 300	< 0.5	–	–

Note:  $\sigma_v$  of the east and south substructures have to be taken as guide values, as well as the masses and radii derived from them.

Table 2 lists the kinematical properties of this complex, composed of a main central cluster surrounded by three substructures. Following the KMM test, we unequivocally associate 9 and 7 galaxies to the south-west and south substructures (see Fig. 7). This allows us to estimate a mean velocity and a rough velocity dispersion to these substructures. So, we obtain a  $\bar{v}_{SW} = 98810 \pm 126$  and  $\bar{v}_S = 99090 \pm 192$  km s<sup>-1</sup> for the mean velocity of the substructures to the SW and S, respectively. In the same way, we estimate a velocity dispersion of  $\sigma_{main} = 999 \pm 160$ ,  $\sigma_{SW} = 792 \pm 230$  for the main body (assumed to be composed by 58 galaxies) and the south-west clump, respectively. The 7 galaxies identified in the southern substructure seem to configure a small compact group of galaxies with very low  $\sigma_v$ . In this case, we could only estimate an upper limit of  $\sigma_S < 300$  km s<sup>-1</sup>. Regarding the eastern substructure, we could assume that the mean velocity should be similar to its corresponding BG (99100 km s<sup>-1</sup>), and in agreement to the low galaxy density and the low X-ray emission observed, the velocity dispersion (in this case computed as the *rms*) of these three galaxies is  $\sigma_E \sim 500$  km s<sup>-1</sup>. We obtain velocity dispersion for the east and south substructures as guide values, and only have to be considered in order to extract information about the magnitude and the importance of such galaxy clumps in the context of the whole RXCJ1230 cluster.

Given that galaxies are tracers of the gravitational potential of a halo, it is possible to estimate the dynamical mass of a system from its velocity dispersion. We use the calculated  $\sigma_v$  and its relation with  $M_{200}$ <sup>8</sup> to determine the dynamical mass of RXCJ1230 and its substructures. In the literature, there are many scaling relations to obtain dynamical masses of clusters from their velocity dispersion. Some examples are that obtained by Evrard et al. (2008), Saro et al. (2013), Munari et al. (2013) and Ferragamo et al. (2020). All of them produce very similar values for the dynamical mass. However, in this work, we follow Munari et al.'s (2013) prescription (see Eq. 1 therein) given that the relation they obtain is constructed using very complete simulations, which take into account not only dark matter particles but also subhaloes, galaxies and AGN feedback. Therefore, following Munari et al. (2013)  $\sigma_v - M_{200}$  relation, we find dynamical masses of  $M_{200} = 9.0 \pm 1.5 \times 10^{14} M_{\odot}$  and  $4.4 \pm 3.3 \times 10^{14} M_{\odot}$  for the main cluster and the south-west substructure, respectively. Regarding the eastern substructure, the velocity dispersion estimate is very unaccurate, which makes very difficult to determine

its mass with a minimum of precision. However, applying the same technique we obtain a rough estimate of  $\sim 1 \times 10^{14} M_{\odot}$  for the eastern clump. In order to compare these values with others in the literature (which mainly refer to  $M_{500}$ ),  $M_{200}$  can also be converted into  $M_{500}$  following the relation given by Duffy et al. (2008).  $M_{500}$  has been rescaled from  $M_{200}$  assuming a concentration parameter  $c = 3.5$  (an appropriate value for clusters at  $z = 0.3$  and  $M_{200} = 10^{14} - 10^{15} M_{\odot}$ ), integrating a Navarro-Frenk-White (NFW) profile (Navarro et al. 1997) and interpolating to obtain  $M_{500}$ . So, we obtain  $M_{500} = 5.6 \pm 1.0 \times 10^{14} M_{\odot}$  and  $2.7 \pm 2.0 \times 10^{14} M_{\odot}$  for the main cluster and the south-west substructure, respectively, and a rough (and qualitative) value of  $\sim 0.7 \times 10^{14} M_{\odot}$  for the eastern clump.

In addition to the mass, we can also estimate the virial radius,  $r_{200}$ , which provides information about the quasi-virialized region, as the radius of a sphere of mass  $M_{200}$  and 200 times the critical density of the Universe at the redshift of the system,  $200\rho_c(z)$ . So,  $M_{200} = 100r_{200}^3 H(z)^2 / G$ . Following this expression we obtain  $r_{200} \sim 1.8$  and  $\sim 1.5 h_{70}^{-1}$  Mpc for the main body and the south-west substructure, respectively. We compile the radius and mass estimates in table 2.

As for the whole mass of the system, the contribution of the east and south groups is of minor importance since they likely have low velocity dispersion and  $M_{200}$  scales with  $\sigma_v^3$ . Thus, we can estimate a reliable total mass of the cluster as the sum of the main body and the other substructures. So, we obtain a total mass of  $M_{200} \simeq 1.4 \pm 0.4 \times 10^{15} M_{\odot}$ .

To summarize, RXCJ1230 is composed of a central main body accreting three substructures from its environment. The main substructure is the one to the south-west, which keeps a mass ratio about 2:1 respect the main cluster. The substructure to the east is very small, since the velocity dispersion and mass estimate show a mass ratio about 10:1 with respect to the main body. Something similar may occur with the southern substructure, which seems to be a very compact group with very low velocity dispersion. Since we are not able to compute accurate velocity dispersion for E and S clumps, the values reported in Tab. 2 for these overdensities have to be taken as qualitative results. However, they are important in order to characterize these minor subclumps. In fact, these findings agree with that obtained by Böhringer et al. (2022) from X-ray data, which supports these results.

#### 4.1. Comparison with X-ray observations

By analysing X-ray data, Böhringer et al. (2022) also find a complex configuration of substructures around the main body of the cluster, which is elongated toward the south. The main sub-

<sup>8</sup>  $r_{200}$  is defined as the radius inside which the average mass density in the cluster is 200 times the critical density of the Universe at the cluster redshift. Similarly to  $r_{500}$  for its corresponding mass density. Therefore,  $M_{200}$  and  $M_{500}$  are the virial mass contain within  $r_{200}$  and  $r_{500}$ , respectively.



structure is placed to the south-west, while another minor clump is detected toward the east.

The detailed X-ray analysis of the RXCJ1230 complex is presented in Böhringer et al. (2022). To summarize, they find that the X-ray temperature of the main body is  $4.7 \pm 0.4$  keV, while the south-west and east components show a  $T_X = 4.4 \pm 0.6$  and  $3.3 \pm 0.6$  keV, respectively. On the other hand, Böhringer et al. (2022) calculate the mass gas inside  $r_{500}$ , 3.45, 2.98 and 2.39 arcmin for the central, south-west and east cluster components, respectively, and use a  $\beta$ -model for the plasma density distribution. They assume a fix  $\beta$ -value of 2/3, which is typical for massive relaxed clusters. Finally, they adopted several scaling relations with  $L_X$ ,  $T_X$ ,  $Y_X$  and  $M_{gas}$  and of  $M_{500}(\beta_{fix})$  and find a total mass of  $M_{500,X} = 7.7(\pm 0.7) \times 10^{14} M_\odot$ .

The sum of dynamical masses corresponding to the main body and south-west clumps, the two main systems of RXCJ1230, is  $M_{500,dyn} \approx 9.0 \pm 2.3 \times 10^{14} M_\odot$ . Therefore, comparing this value with that derived from X-ray, we see that  $M_{500,dyn}$  and  $M_{500,X}$  are in agreement within errors and they differ by about 15%.

Comparing the mass of individual clumps, Böhringer et al. (2022) find a  $M_{500,X} = 3.7 \pm 0.5 \times 10^{14} M_\odot$  within  $r_{500}$  in the main cluster, while we obtain  $M_{500,dyn} = 5.6 \pm 1.0 \times 10^{14} M_\odot$ . This discrepancy of about 30% may come from the fact that  $M_{500,dyn}$  has been derived by converting  $M_{200}$  into  $M_{500}$ . In fact, when considering only the 47 galaxy members with redshift within  $r_{500}$  ( $=3.45$  arcmin  $=1$  Mpc; see Tab. 3 in Böhringer et al. 2022), a  $\sigma_v = 913 \pm 133$  km s $^{-1}$  is obtained, which points to a mass of about  $M_{500,dyn} \sim 4.3 \times 10^{14} M_\odot$ , almost coincident with that derived from X-ray data. For the south-west component we find a good agreement of the mass determination with  $M_{500,X} = 2.5 \pm 0.6 \times 10^{14} M_\odot$  from X-rays and  $M_{500,dyn} = 2.7 \pm 2 \times 10^{14} M_\odot$  from the galaxy dynamics. For the eastern component a mass estimate is more difficult. However, even considering rough estimations,  $M_{500,dyn} \sim 1 \times 10^{14} M_\odot$  and  $M_{500,X} = 1.35 \pm 0.3 \times 10^{14} M_\odot$  roughly agree within errors.

## 5. Dynamics and merging

As we pointed out above, both the main cluster and the three substructures are well detectable and optical and X-ray data indicate very similar locations, so we are looking at RXCJ1230 in a prior merging phase. However, the velocity distribution and the not so well resolved galaxy populations suggest that the substructures start to interact with the main cluster. With this scenario, the main collision will be produced between the substructure to the south-west involving a mass ratio of 2:1. In fact, the X-ray temperatures of the main body and the substructure are very similar,  $T_{X,C} = 4.7 \pm 0.4$  and  $T_{X,SW} = 4.4 \pm 0.6$  keV (Böhringer et al. 2022) for the central main clump and the south-west substructure, respectively, even if they show very different dynamical masses. Whereas typical X-ray temperatures of relaxed clusters with  $M_{500} \sim 2.7 \times 10^{14} M_\odot$  are about 3 keV (see e.g. Fig. 9 in Kettula et al. 2013, and references therein), the south-west substructure, could be starting to show an enhancement of its intra-cluster medium (ICM) temperature. This enhancement supports the fact that the main body and south-west substructure are starting to collide.

When the merging scenario is assumed to explain an enhancement of the ICM temperature, a relative colliding velocity is needed to heat up the ICM (Gutierrez & Krawczynski 2005). On the assumption that the two components are to cause a head-on collision and that their kinetic energies are completely converted to thermal energy, the colliding velocity is

$v_{coll}^2 = 3k\Delta T/\mu m_p$  km s $^{-1}$ , following prescriptions detailed in Shibata et al. (1999), where  $\mu$  and  $m_p$  are the mean molecular weight (0.6) in amu, and the proton mass, respectively. So, assuming an excess temperature of  $k\Delta T \sim 1.5$  keV, we find a  $v_{coll} \approx 850$  km s $^{-1}$ , which is in very good agreement with the observed relative LOS velocity in the cluster rest frame, as computed from  $(\bar{v}_C - \bar{v}_{SW})/(1+z) = 869$  km s $^{-1}$ .

### 5.1. Two body merging model

In this section, we investigate the relative dynamics of RXCJ1230 main body (C) and its main substructure, the south-west (SW) one, which dominates the dynamics of the whole cluster, with a mass ratio about 2:1. The rest of the interactions, including the south and east substructures, are minor merger events with mass ratios about 10:1. We analyze this C-SW interaction from different approaches, which are based on an energy integral formalism in the framework of locally flat spacetime and Newtonian gravity (see e.g. Beers et al. 1982). The three relevant observable quantities for the two system interaction are: the relative line-of-sight velocity,  $V_r = 869 \pm 153$  km s $^{-1}$ ; the projected physical distance,  $D = 0.97 h_{70}^{-1}$  Mpc (3.38 arcmin); and the total mass of the two systems by adding the masses of the two clumps within  $r_{200}$ ,  $M_{sys} \sim 13.4 \pm 3.6 \times 10^{14} M_\odot$  (see Sect. 4).

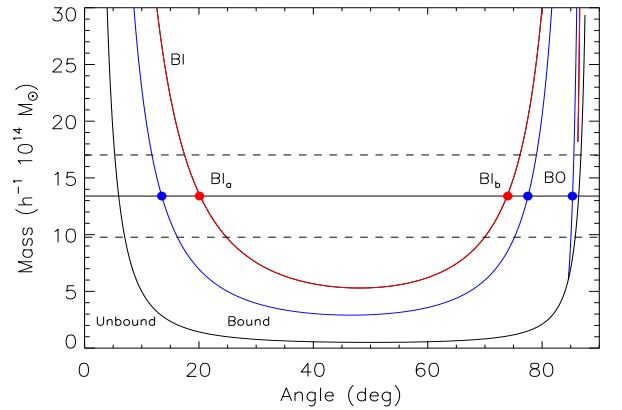


**Fig. 8.** Two-body model applied to the main cluster and south-west galaxy substructure (C-SW system). The black curve separates bound and unbound regions according to the Newtonian criterion. Solid curves represent the bound incoming (BI) and bound outgoing (BO) solutions. Blue and red curves denote the models for 706 and 1022 km s $^{-1}$ , which represent the marginal relative velocity between main cluster and substructure, considering the corresponding uncertainties. The horizontal lines represent the observational values of the total mass of the C-SW system, with it uncertainty (dashed lines).

First, we consider the Newtonian criterion for the gravitational binding, which follows the expression  $V_r^2 D \leq 2GM_{sys} \sin^2 \alpha \cos \alpha$ , where  $\alpha$  is the projection angle between the line connecting the centres of the two clumps and the plane of the sky. Fig. 8 represents the two-body model obtained. Considering the value of  $M_{sys}$ , the C-SW system is bound between  $6^\circ$  and  $86^\circ$  with a probability of  $\int_{6^\circ}^{86^\circ} \cos \alpha d\alpha = 0.89$  (i.e. 89%).

Then, we apply the analytical two-body model introduced by Beers et al. (1982) and Thompson (1982) (see also Lubin et al. 1998). This model assumes radial orbits and not rotation of the system. In addition, the clumps are assumed to start their evolution at  $t_0 = 0$  with a separation of  $d_0 = 0$  and are moving apart or

coming together for the first time in the history. That is, with this model, we are assuming that we are seeing the cluster prior to collision (at  $t = 9.98$  Gyr at the redshift of RXCJ1230). The solutions for this model is shown in Fig. 8, where we compare the total mass of the system,  $M_{\text{sys}}$ , with the projection angle,  $\alpha$ . The possible solutions span several cases: two bound incoming solutions ( $\text{BI}_a$  and  $\text{BI}_b$ ) around  $14^\circ$ - $20^\circ$  and  $74^\circ$ - $77^\circ$ , respectively, and one bound outgoing (BO) at  $\sim 85^\circ$ . The incoming case is degenerated because of the ambiguity in the projection angle  $\alpha$ . So, for simplicity, we assume the mean value in the incoming cases, which is  $\text{BI}_a \sim 17^\circ$  and  $\text{BI}_b \sim 76^\circ$  and that the region of  $M_{\text{sys}}$  values are equally probable for individual solutions. Under these assumptions we estimate the following probabilities:  $P_{\text{BI}_a} \sim 87\%$ ,  $P_{\text{BI}_b} \sim 13\%$  and  $P_{\text{BO}} \ll 0.1\%$ . We discard the BO solution because it is very unlikely and we analyse below the BI ones.

Between the two possible incoming solutions,  $\alpha = 17^\circ$  and  $\alpha = 76^\circ$ , the second one is quite unlikely. An  $\alpha = 76^\circ$  (associated to the  $\text{BI}_b$  solution) would imply a distance between clumps of  $\sim 4.0 h_{70}^{-1}$  Mpc, which more than twice  $r_{200}$ . On the other hand, an  $\alpha = 17^\circ$  ( $\text{BI}_a$ ) is the most likely solution and, for this case, the distance C-SW centres would be  $\sim 1.0 h_{70}^{-1}$  Mpc, which would explain a certain degree of interaction. Thus, when assuming  $\alpha = 17^\circ$  the colliding velocity would be  $\sim 3000 \text{ km s}^{-1}$  and the cluster clumps will cross after  $\sim 0.3$  Gyr.

For sure, the characterization of the dynamics of RXCJ1230 through these models is affected by several limitations. First, the two-body model does not consider the possibility of an off-axis merger neither a mass distribution in the subclusters. And secondly, this study does not take into account the presence of minor subclusters (the south and east clumps). Therefore, the model here presented has to be taken as one of the many possible approaches to the collision scenario in RXCJ1230.

## 6. Summary and conclusions

We present the results of the kinematical and dynamical state of the complex galaxy cluster RXCJ1230.7+3439. Our study is based on new spectroscopic redshifts acquired at the 3.5m TNG telescope covering a region of  $\sim 8' \times 8'$ . We also consider some SDSS DR16 spectroscopic redshifts in order to complement our sample. In addition, we use the SDSS photometry in a field of  $\sim 13' \times 10'$  to analyse the spatial distribution of likely cluster members.

We select 77 galaxy cluster members around  $z = 0.332$  and compute a LOS global velocity dispersion of  $\sigma_v = 1004^{+147}_{-122} \text{ km s}^{-1}$ .

Our analysis confirms the presence of three substructures surrounding the main body of the cluster and they are well recognizable in the plane of the sky in the 2D spatial distribution of galaxies. Moreover, we identify several bright galaxies dominating the core of each substructure. The more massive substructure is the one located to the south-west, which shows a  $\sigma_v \sim 800 \text{ km s}^{-1}$  and differs by  $\sim 870 \text{ km s}^{-1}$  from the main body in the LOS velocity. The southern substructure resembles a compact group of galaxies with very low velocity dispersion ( $\sigma_s < 300 \text{ km s}^{-1}$ ), while we find that the eastern substructure shows a  $\sigma_E \sim 500 \text{ km s}^{-1}$ . The dynamical masses estimated from these velocity dispersions are  $M_{200} = 9.0 \pm 1.5 \times 10^{14} M_\odot$ ,  $4.4 \pm 3.3 \times 10^{14} M_\odot$  and  $\sim 1 \times 10^{14} M_\odot$  for the main cluster, the south-west and east substructures, respectively. Thus, considering the complex structure of RXCJ1230, we estimate that the whole cluster contains a total mass in the range of  $M_{200} \simeq 1.4 \pm 0.4 \times 10^{15}$ .

Given that the galaxy density peaks coincide with those observed in the X-ray surface brightness, we infer that the system agrees with a pre-merging event, where the main collision is that involving the main body and the south-west clump. This interaction occurs with a mass ratio of 2:1 and an impact velocity of  $\Delta v_{\text{rf}} \sim 3000 \text{ km s}^{-1}$ . The most likely solution obtained from a two-body problem for these two systems suggests that the merging axis lies at  $\sim 17^\circ (\pm 3^\circ)$  with respect to the plane of the sky and the systems will be completely joined in about 0.3 Gyr. However, a slightly increase of the X-ray temperature ( $k\Delta T \sim 1.5 \text{ keV}$ ) in the south-west may indicate that we are observing a certain degree of interaction.

### Acknowledgements.

We thank to the referee for his useful comments, which have really helped the authors to improve this work.

R. Barrena acknowledges support by the Severo Ochoa 2020 research programme of the Instituto de Astrofísica de Canarias. H. Böhringer acknowledges support from the Deutsche Forschungsgemeinschaft through the Excellence cluster "Origins". G. Chon acknowledges support by the DLR under the grant n° 50 OR 1905.

This article is based on observations made with the Italian Telescopio Nazionale Galileo operated by the Fundación Galileo Galilei of the INAF (Istituto Nazionale di Astrofisica). This facility is located at the Spanish del Roque de los Muchachos Observatory of the Instituto de Astrofísica de Canarias on the island of La Palma.

Funding for the Sloan Digital Sky Survey (SDSS) has been provided by the Alfred P. Sloan Foundation, the Participating Institutions, the National Aeronautics and Space Administration, the National Science Foundation, the U.S. Department of Energy, the Japanese Monbukagakusho, and the Max Planck Society.

The Pan-STARRS1 Surveys (PS1) and the PS1 public science archive have been made possible through contributions by the Institute for Astronomy, the University of Hawaii, the Pan-STARRS Project Office, the Max-Planck Society and its participating institutes, the Max Planck Institute for Astronomy, Heidelberg and the Max Planck Institute for Extraterrestrial Physics, Garching, The Johns Hopkins University, Durham University, the University of Edinburgh, the Queen's University Belfast, the Harvard-Smithsonian Center for Astrophysics, the Las Cumbres Observatory Global Telescope Network Incorporated, the National Central University of Taiwan, the Space Telescope Science Institute, the National Aeronautics and Space Administration under Grant No. NNX08AR22G issued through the Planetary Science Division of the NASA Science Mission Directorate, the National Science Foundation Grant No. AST-1238877, the University of Maryland, Eotvos Lorand University (ELTE), the Los Alamos National Laboratory, and the Gordon and Betty Moore Foundation.

## References

- Allen, S. W., Evrard A.E., Mantz A.B. 2011, ARA&A, 49, 409
- Appenzeller, I., Thiering I., Zickgraf F. J., 1998, ApJS, 117, 319
- Ashman, K. M., Bird C. M., Zepf S. E., 1994, AJ, 108, 2348
- Barrena, R., Boschin W., Girardi M., et al., 2007, A&A, 467, 37
- Barrena, R., Girardi M., Boschin W., et al., 2012, A&A, 540, A90
- Beers, T. C., Geller M. J., Huchra J. P., 1982, ApJ, 257, 23
- Beers, T. C., Flynn K., Gebhardt K., 1990, AJ, 100, 32
- Biviano, A. 2000, IAP 2000 meeting, Florence Durret & Daniel Gerbal Eds.
- Böhringer, H., Voges, W., Huchra, J. P., 2000 ApJS, 129, 435
- Böhringer, H., Werner, N., 2010, A&A Rev., 18 (1-2), 127
- Böhringer, H., Chon, G., Ellis, R. S., et al., 2022, A&A, in preparation
- Dressler, A., Shectman, S. A., 1988, AJ, 95, 985
- Duffy, A. R., Schaye, J., Kay, S. T., et al., 2008, MNRAS, 390, L64
- Eales, S. A., Baes, M., Bourne, N., et al., 2018, MNRAS, 481, 1183
- Evrard, A. E., Blalek, J., Busha, M., et al., 2008, ApJ, 672, 122
- Ferragamo, A., Rubiño-Martín, J. A., Betancort-Rijo, J., et al., 2020, A&A, 641, A41
- Gal, R. R., del Carvalho, R. R., Lopes, P. A., A., 2003, AJ, 125, 2064
- Golovich, N., Dawson, W. A., Wittman, D. M., et al., 2019, ApJS, 240, 39
- Gutierrez, K., Krawczynski, H., 2005, ApJ, 619, 161
- Hao, J., McKay, T. A., Koester, B. P., et al., 2010, ApJS, 191, 254
- Boschin, W., Girardi, M., Barrena, R. 2013, MNRAS, 434, 772
- Kennicutt, R. C., 1992, ApJS, 79, 255
- Kettula, K., Finoguenov, A., Massey, R., et al., 2013, ApJ, 778, 74
- Laganá, T. F., Lima Neto, G. B., Andrade-Santos, F., et al., 2008, A&A, 485, 633
- Loewenstein, M., Origin and Evolution of the Elements, 2003, Cambridge University Press, 4, 422 (also arXiv:astro-ph/0310557)
- Lubin, L. M., Postman, M., Oke, J. B., 1998, AJ, 116, 643

- Mamon, G., Biviano, A., Murante, G. 2010, *A&A*, 520, A30
- Munari, E., Biviano, A., Borgani, S., et al. 2013, *MNRAS*, 430, 2638
- Navarro, J. F., Frenk, C. S., White, S. D. M., 1997, *ApJ*, 490, 493
- Planck Collaboration XXVII, *A&A*, 594, A27
- Ribeiro, A. L. B., Lopes, P. A. A., Trevisan, M. 2011, *MNRAS*, 413, L81
- Roettiger, K., Loken, C., Burns, J. O. 1997, *ApJS*, 109, 307
- Saro, A., Mohr, J. J., Bazin, G., et al., 2013, *ApJ*, 772, 47
- Schlegel, D. J., Finkbeiner, D. P., Davis, M., 1998, *ApJ*, 500, 525
- Shibata, R., Honda, H., Ishida, M., et al., 1999, *ApJ*, 524, 603
- Springel, V., 2005, *MNRAS*, 364, 1105
- Thompson, L. A., 1982, in *IAU Symp.*, 104, Early Evolution of the Universe and the Present Structure, ed. G.O. Abell, & G. Chincarini (Dordrecht: Reidel)
- Tonry, J., Davis, M. 1979, *ApJ*, 84, 1511
- Umetsu, K., 2000, *A&A Rev.*, 28 (I), id. 7
- van Weeren, R. J., de Gasperin, F., Akamatsu, H., et al., 2019, *Space Sci. Rev.*, 215:16
- Wen, Z. L., Han, J. L., Liu, F. S., 2009, *ApJS*, 183, 197